Operando metalloid Znδ+ active sites for highly efficient carbon dioxide reduction electrocatalysis

A Journal of the Gesellschaft Deutscher Chemiker

Angewandte International Edition GDCh Chemie

www.angewandte.org

Accepted Article

Title: Operando Metalloid Znδ+ Active Sites for Highly Efficient Carbon Dioxide Reduction Electrocatalysis

Authors: Xin Yu Zhang, Wen Jing Li, Jiacheng Chen, Xue Feng Wu, Yuan Wei Liu, Fangxin Mao, Hai Yang Yuan, Minghui Zhu, Sheng Dai, Hai Feng Wang, P. Hu, Chenghua Sun, Peng Fei Liu, and Huagui Yang

To be cited as: *Angew. Chem. Int. Ed.* **2022**, e202202298

Link to VoR: https://doi.org/10.1002/anie.202202298

WILEY-VCH

10.1002/anie.202202298

WILEY-VCH

RESEARCH ARTICLE

Operando Metalloid $Zn^{\delta+}$ Active Sites for Highly Efficient Carbon Dioxide Reduction Electrocatalysis

Xin Yu Zhang,[a,‡] Wen Jing Li,[a,‡] Jiacheng Chen,[b] Xue Feng Wu,[a] Yuan Wei Liu,[a] Fangxin Mao,[a] Hai Yang Yuan,[a,*] Minghui Zhu,[b] Sheng Dai,[c] Hai Feng Wang,[d] P. Hu,[d,e] Chenghua Sun,[f] Peng Fei Liu,[a,*] and Hua Gui Yang[a,*]

[a] Dr. X. Y. Zhang, W. J. Li, X. F. Wu, Y. W. Liu, Dr. F. Mao, Dr. H. Y. Yuan, Dr. P. F. Liu, Prof. H. G. Yang
Key Laboratory for Ultrafine Materials of Ministry of Education
Shanghai Engineering Research Center of Hierarchical Nanomaterials
School of Materials Science and Engineering
East China University of Science and Technology
130 Meilong Road, Shanghai, 200237 (China)
E-mail: hgyang@ecust.edu.cn; pfliu@ecust.edu.cn; hyyuan@ecust.edu.cn
[b] J. Chen, Prof. M. Zhu
State Key Laboratory of Chemical Engineering
School of Chemical Engineering
East China University of Science and Technology
130 Meilong Road, Shanghai, 200237 (China)
[c] Prof. S. Dai
Key Laboratory for Advanced Materials and Feringa Nobel Prize Scientist Joint Research Center
Institute of Fine Chemicals
School of Chemistry and Molecular Engineering
East China University of Science and Technology
130 Meilong Road, Shanghai, 200237 (China)
[d] Prof. H. F. Wang, Prof. P. Hu
Key Laboratory for Advanced Materials, Centre for Computational Chemistry and Research Institute of Industrial Catalysis
School of Chemistry and Molecular Engineering
East China University of Science and Technology
130 Meilong Road, Shanghai, 200237 (China)
[e] Prof. P. Hu
School of Chemistry and Chemical Engineering
The Queen's University of Belfast
Belfast BT9 5AG (UK)
[f] Prof. C. Sun
Department of Chemistry and Biotechnology
Center for Translational Atomaterials
Swinburne University of Technology
Hawthorn, VIC, 3122 (Australia)
[‡] These authors contributed equally to this work.

Abstract: Electrochemical CO_2-to-CO conversion provides a promising way to solve problems of greenhouse effect; however, developing low-cost electrocatalysts to mediate high-efficiency CO_2 reduction remains a grand challenge on account of the limited understanding in the real active sites. Herein, we revealed the operando $Zn^{\delta+}$ metalloid sites as the real active sites of stable nonstoichiometric ZnO_x structure derived from $Zn_2P_2O_7$ through operando X-ray absorption fine structure analysis in conjunction with evolutionary-algorithm-based global optimization method, which exhibited excellent performance for CO_2-to-CO electrocatalysis. Furthermore, theoretical and experimental results demonstrated that $Zn^{\delta+}$ metalloid active sites could facilitate the activation of CO_2 and the hydrogenation of $*CO_2$, thus accelerating the CO_2-to-CO conversion. Our work establishes a critical fundamental understanding of the origin of the real active center in the zinc-based electrocatalysts for CO_2 reduction reaction.

Introduction

Electrochemical CO_2 reduction reaction (CO_2RR) is an appealing scheme to store intermittent solar- and wind-powered electricity in carbon-based chemicals and fuels, including CO, formate, methane, ethylene, and other long alkyl chains[1]. Among the diverse CO_2RR pathways, CO_2-to-CO conversion is one of the most promising practices due to its high selectivity and facile separation from liquid water[2]. However, practical CO_2-to-CO electrolysis requires a catalyst to react at high selectivity and high rate with low overpotentials (η), which still relies on noble metal-based nanomaterials (*e.g.*, gold and silver)[3]. Very recently, the molecular catalyst has been reported to catalyze CO_2-to-CO conversion at a current density (j) of -150 mA cm^{-2} with Faradaic efficiency (FE) > 95% in a zero-gap membrane flow cell[4]; moreover, several examples of atomically or molecularly dispersed electrocatalysts have demonstrated FE_{CO} > 90% at the operated j over -100 mA cm^{-2}[5]. Unfortunately, traditional solid-state, low-cost electrocatalysts have not generally achieved significant improvements in the efficiencies and selectivities at high current densities, which remains a big challenge in this field.

Low-cost and earth-abundant electrocatalysts based on nanostructured zinc (Zn) have shown great promise for CO_2-to-CO conversion[6]. Modifications to Zn-based electrocatalysts, *e.g.*, engineering crystal facets[7], tuning morphologies and components[8,9], constructing single-atom catalysts (SACs)[10], or introducing lattice defects and ligands[11,12], have been

implemented to improve CO_2-to-CO activity. However, on certain Zn nanostructures, partial current densities of CO (j_{CO}) are usually lower than -20 mA cm^{-2} even at high η (> 900 mV)[13]. One pain point lies in the *in-situ* reconstruction of the pristine well-designed active structures for the most solid-state CO_2RR electrocatalysts under operando electrolysis conditions, and their catalytic performances are often limited by how to keep or *in-situ* generate these active structures. For example, positively-charged metal sites can boost the CO_2 activation process with ultrahigh activities[13,14], but it is extremely difficult to preserve oxidation states under the potential regions of CO_2 electroreduction[15]. Recently, K. Daasbjerg et al. reported a nitrogen-anchored low-valence Zn-based SAC showing excellent performance for electrochemical CO_2-to-CO conversion, which revealed the relationship between valence state and catalytic performance of Zn-based catalysts[16]. Furthermore, due to the negative electroreduction potential and complex solution environment in the electrocatalytic process, it is untoward to reveal the operando active sites at atomistic- and molecular-level and the catalytic mechanism of electrocatalysts during the CO_2RR process, hence limiting the rational design and development of catalysts with high selectivity, activity, and stability[17]. With these in mind, we anticipate it will be a breakthrough to develop stable positively-charged $Zn^{\delta+}$ sites (*e.g.*, nonstoichiometric ZnO_x) under operando reduction potentials for high-current-density CO_2 electrolysis at low overpotentials, and to further reveal the active sites and performance enhancement mechanisms at the atomic scale.

Herein, we develop zinc pyrophosphate ($Zn_2P_2O_7$) as a low-cost and efficient precatalyst, which can operando generate nonstoichiometric ZnO_x with stable low-valent $Zn^{\delta+}$ sites to motivate high-current-density CO_2-to-CO at low overpotentials. This resultant catalyst can produce CO at -300 mA cm^{-2} with FE_{CO} of 98.9%, and deliver a high j_{CO} up to -441 mA cm^{-2} at a low potential of ~870 mV in a flow cell, which is among the best of the developed CO_2-to-CO electrocatalysts. These performance merits have been further integrated with a zero-gap anion membrane electrode assembly (MEA), in which this catalyst achieves a full-cell energy efficiency (EE) of 58.0% at -100 mA cm^{-2}. Our operando experimental characterizations demonstrate that the stable ZnO_x structure derived from $Zn_2P_2O_7$ during electroreduction leads to high-efficiency CO_2-to-CO conversion performance. Through Universal Structure Predictor Evolutionary Xtallography (USPEX), we successfully predict the real active sites of stable ZnO_x structure derived from $Zn_2P_2O_7$ at atomistic-level, and further density functional theory (DFT) calculation in conjunction with *in-situ* surface-enhanced infrared absorption spectroscopy (SEIRAS) testify that operando $Zn^{\delta+}$ metalloid active sites on the surface of ZnO_x are conducive to the activation of CO_2 and the formation of *COOH, a key intermediate for the CO production. All the results unveil metalloid $Zn^{\delta+}$ species as the highly active sites for CO_2-to-CO conversion, and we believe this work may not only provide an effective operando-derivative strategy for designing low-cost electrocatalysts but also provide a new understanding of the activity origin of Zn-based electrocatalysts toward highly efficient electroreduction of CO_2-to-CO.

Results and Discussion

Transition metal phosphates have been reported to give a positive contribution to structural stability, on account of that the structural flexibility of the $(P_2O_7)^{4-}$ group could stabilize the intermediate states of Zn by changing their local positions with ease[18]. Based on this, we speculate it will provide possibilities for generating stable positively-charged $Zn^{\delta+}$ sites on the surface when $Zn_2P_2O_7$ is taken as a precatalyst, contributing to an effective CO_2RR performance. First and foremost, we simulated the reaction thermodynamic energy of $Zn_2P_2O_7$ and ZnO being reduced to metallic Zn, respectively (see details in Supporting Information). As shown in Figure 1a, $Zn_2P_2O_7$ is reduced to Zn with positive Gibbs free energy (> 0 eV) within the operating potential range of CO_2-to-CO reaction, which indicates that the catalyst is difficult to be entirely reduced to pure-Zn, thus endowing a possibility to form ZnO_x structure on the surface. On the contrary, ZnO is easily reduced to the pure-Zn phase because of its structural instability, leading to the lack of $Zn^{\delta+}$ sites, which is adverse to the improvement of the electrocatalytic activity. On this basis, we rationally prepared $Zn_2P_2O_7$ precatalysts *via* a facile sol-gel method (see more details in Supporting Information), and we could obtain gram-scale products through a one-off preparation process in the lab-scale (Figure S1). X-ray diffraction (XRD) was conducted to analyze the crystalline structures of $Zn_2P_2O_7$. As shown in Figure 1b, the diffraction peaks of the synthesized sample are well indexed to the monoclinic phase of $Zn_2P_2O_7$ (PDF#97-005-6297), without any impurity. $Zn_2P_2O_7$ features the grey color (inset of Figure 1b) and exhibits a typical thortveitite structure, which exhibits two types of distances between two adjacent Zn atoms (3.3 and 5.5 Å, Figure S2a). For comparison, ZnO control samples were obtained *via* a similar sol-gel process, showing the diffraction peaks of ZnO reference with a hexagonal system (PDF#97-015-5780) in the XRD analysis (Figure S2b, S3). To further analyze the local structure of $Zn_2P_2O_7$, X-ray absorption fine structure spectroscopy (XAFS) was conducted. As shown in Figure 1c, the X-ray absorption near edge structure (XANES) spectrum of Zn *K*-edge shows that the bulk Zn ions in $Zn_2P_2O_7$ keep in +2 oxidation states. Furthermore, its Fourier-transformed extended X-ray absorption fine structure (EXAFS) is also illustrated in Figure 1d. The first peak centered at ~1.5 Å (without phase correction if not mentioned) is assigned to Zn-O bonds[13]. The second distinct peak at ~2.8 Å is attributed to Zn-P bonds in the structure. Fourier transformed infrared (FTIR) spectroscopy was further carried out to confirm the chemical bonds in the sample (Figure S4), showing characteristic peaks in the frequency range of 1100-900 cm^{-1}, which are assigned to asymmetric and symmetric P-O bonds. The asymmetric P-O-P bridge vibration is also observed[19]. Scanning electron microscopy (SEM) was conducted to analyze the morphology of the obtained samples. In Figure S5a, $Zn_2P_2O_7$ exhibits the irregularly stacked nanoparticles. In the transmission electron microscopy (TEM) image of $Zn_2P_2O_7$ (Figure 1e), interconnected nanoparticles are observed, and the corresponding selected area electron diffraction (SAED) pattern further confirms the high crystallinity of $Zn_2P_2O_7$ (inset of Figure 1e). Moreover, its high-angle annular dark field-scanning transmission electron microscopy (HAADF-STEM) image and the corresponding energy dispersive X-ray spectroscopy (EDS) analysis demonstrates the homogenous dispersions of Zn, O, and P elements in the whole area of $Zn_2P_2O_7$ (Figure 1f). For comparison, SEM and TEM analysis of ZnO nanoparticles were also performed (Figure S5b, S6), showing no significant difference in morphology with $Zn_2P_2O_7$.

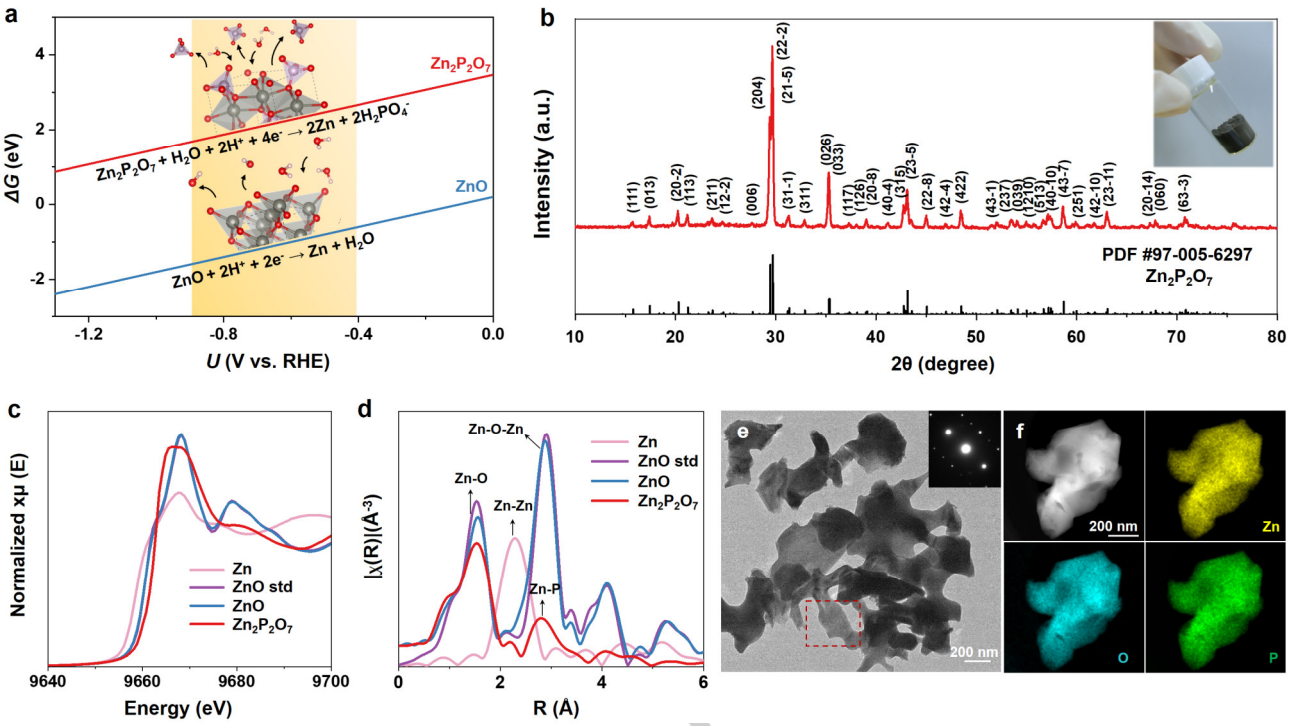

Figure 1. Structural characterization of $Zn_2P_2O_7$ precatalyst. (a) The Gibbs free energy diagram of $Zn_2P_2O_7$ and ZnO reduced to Zn, which varies according to the operating potential. The orange area is the common operating potential range (-0.4 to -0.9 V). (b) XRD pattern of $Zn_2P_2O_7$ sample, which is assigned to PDF#97-015-5780. Inset: Photograph of $Zn_2P_2O_7$ sample. (c, d) XAFS characterization of (c) the normalized Zn *K*-edge XANES spectra and (d) Fourier-transformed Zn *K*-edge EXAFS spectra. (e) TEM image of $Zn_2P_2O_7$. Inset: the corresponding SAED pattern. (f) HAADF-STEM image of $Zn_2P_2O_7$ and the corresponding EDS elemental maps of Zn, O, and P elements, respectively.

To verify the formation rationality of the $Zn^{\delta+}$ species derived from $Zn_2P_2O_7$ catalysts during CO_2RR, a series of characterizations for structural evolution were conducted. Firstly, the XRD analysis before and after CO_2RR indicates that the diffraction peaks of $Zn_2P_2O_7$ disappear and show no sharp peak beside the carbon paper substrate, which might be due to the formation of amorphous species (Figure 2a). However, the diffraction peaks of the metallic Zn appear after CO_2RR for ZnO controls, and trace of ZnO component was ascribed to slight surface oxidation under the air. To study the changes of the valence states for $Zn_2P_2O_7$, X-ray photoelectron spectroscopy (XPS) was conducted. In Figure S7a, the peak in the Zn 2p region of initial $Zn_2P_2O_7$ is ascribed to Zn^{2+} (1022.0 eV), and the Zn 2p region of initial ZnO can be fitted into two constituent peaks, which are ascribed to Zn^{2+} and Zn^0 (1021.3 eV)[20]. After CO_2RR at the applied *j* of -200 mA cm^{-2} for 1 h, the characteristic Zn^0 peak appears with a certain amount of Zn^{2+} still existing in $Zn_2P_2O_7$, indicating the durable existence of surface Zn^{2+} components of the $Zn_2P_2O_7$ sample during CO_2RR. While the Zn^0 peak occupies a dominant position in the ZnO sample with the Zn^{2+} peak disappearing after CO_2RR, which proves that the ZnO is totally reduced to metallic Zn during CO_2RR. Further evidence comes from the O 1s spectrum shown in Figure S7b, and the peaks at the binding energy of 531.5, 533.0, and 535.0 eV in $Zn_2P_2O_7$ can be attributed to the non-bridging oxygen in the phosphate group (P=O), the symmetric bridging oxygen in P-O-P group and the absorbed H_2O, respectively[21]. The O 1s spectrum of $Zn_2P_2O_7$ after CO_2RR shows that the $(P_2O_7)^{4-}$ ions have been leached during the reduction process, accompanied by an emergent Zn-O peak (530.2 eV), which is coincided with the XPS spectra in Zn 2p and P 2p regions (Figure S7c)[9]. As for the ZnO control sample, the peak of Zn-O entirely disappears, indicating the surface Zn^{2+} components are mostly reduced to Zn^0.

We further conducted a time-dependent Raman analysis of $Zn_2P_2O_7$ along with the ZnO control. In Figure 2b, the peaks from 1250 to 950 cm^{-1} belong to the P-O stretching modes of $(P_2O_7)^{4-}$ [22]. As the CO_2RR goes on (at the constant *j* of -400 mA cm^{-2} in 2.0 M KOH), the characteristic peaks of $(P_2O_7)^{4-}$ change, which indicates the possible ions leaching during the electroreduction process. It is mentionable that the emergence of the peaks at about 576, 1073, and 1150 cm^{-1} attributed to the Zn-O finger signal, which proves the generation of oxidized Zn species as the CO_2RR goes on[23]. For comparison, all the finger signals of Zn-O vanish with prolonged CO_2RR time in the ZnO control sample. Meanwhile, we also evaluated the time-dependent CO_2-to-CO selectivity for the two samples at different applied *j*. In Figure 2c, as the reduction reaction continues, the ratio of FE_{CO}(ZnO) to $FE_{CO}(Zn_2P_2O_7)$ gradually decreases, and this phenomenon would be more obvious when applying a higher constant *j*, which demonstrates the importance of oxidized Zn species for CO_2-to-CO activity.

To further understand the oxidation state evolution in catalysts during CO_2RR, operando XAFS measurements were performed using the home-built device (see details in Supporting Information and Figure S8). Firstly, the XANES spectra of $Zn_2P_2O_7$-OCV and ZnO-OCV were collected after 1.0 M KOH electrolyte circulated into the cell. Once the cathodic *j* was applied, the XANES profile of the ZnO sample occurred a distinct change

10.1002/anie.202202298

and kept metallic Zn^0 state in 5 min, while $Zn_2P_2O_7$ maintained in higher valence states than metallic Zn^0 in the whole course of CO_2RR up to 35 min (Figure 2d). The corresponding linear combination fitting (LCF) results demonstrated that the majority of $Zn_2P_2O_7$ (69.8%) was in the Zn^{2+} oxidation state after 5 min, while Zn^{2+} had been decreased to 16.0% in the ZnO control sample, which reveals that the transition between Zn^{2+} and Zn^0 for ZnO is more rapid (Figure 2e). After that the $Zn_2P_2O_7$ catalyst had been electrochemically reduced *via* CO_2RR for 35 min, it still maintained 22.2% composed of the Zn^{2+}, which unambiguously demonstrates the stable existence of ZnO_x species during the CO_2 gas diffusion electrolysis. Figure 2f exhibits the operando EXAFS spectra, the enhancement of Zn-Zn peak (~2.3 Å), and the reduction of Zn-O peak (~1.5 Å) in samples (solid lines) suggested the Zn^{2+} in catalysts gradually reduced to metallic Zn^0 when CO_2RR took place[24]. After that $Zn_2P_2O_7$ had been electrochemically reduced *via* CO_2RR for 35 min, it still showed a higher Zn-O coordination number compared with ZnO control, indicating the generation of low-valent ZnO_x derived from $Zn_2P_2O_7$.

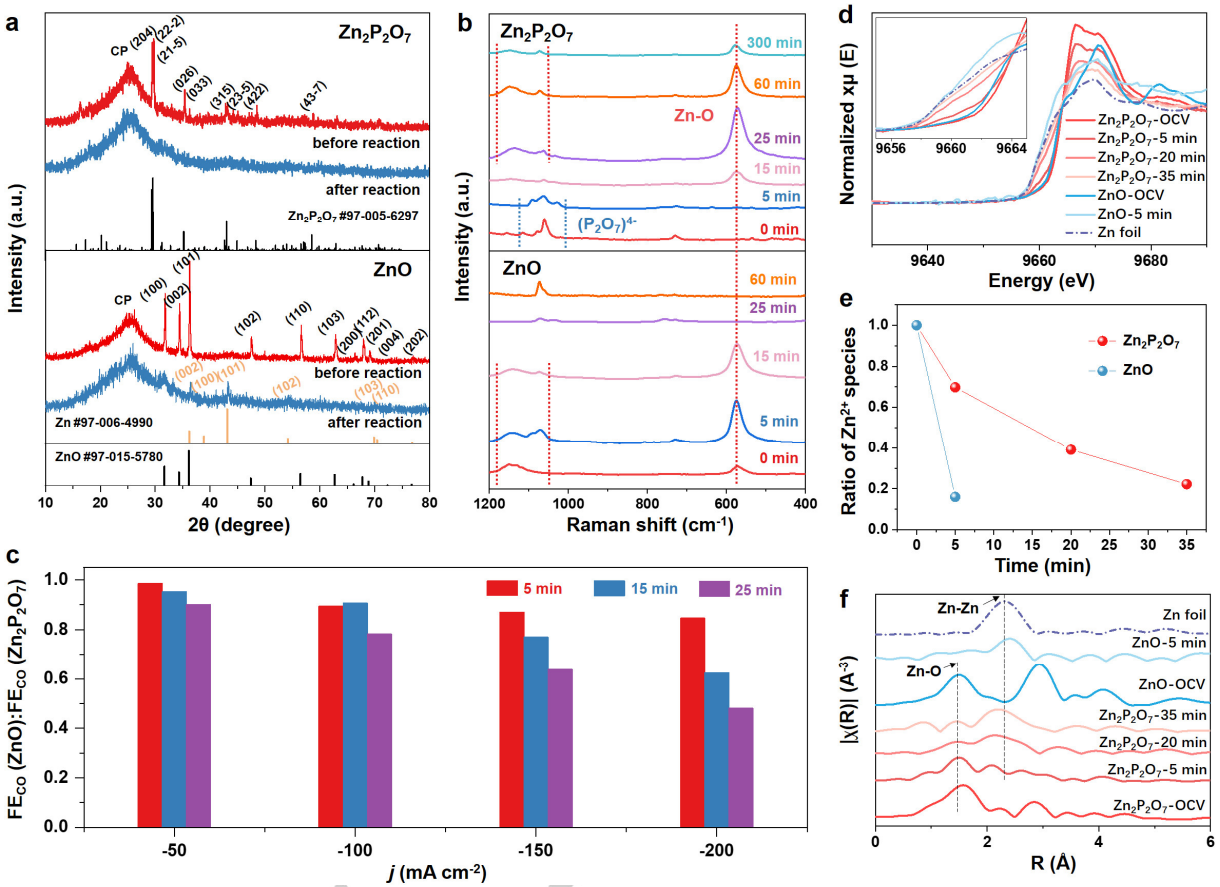

Figure 2. Structural evolution investigation of electrocatalysts during CO_2RR. (a) XRD patterns of $Zn_2P_2O_7$ and ZnO control coated on carbon paper before and after CO_2RR, which indicates that ZnO would be reduced to metallic Zn under reduction potential. (b) Raman spectra of $Zn_2P_2O_7$ and ZnO control coated on carbon paper corresponding to different reaction times at an applied current density of -400 mA cm^{-2} in a flow cell reactor with 2.0 M KOH as the electrolyte, indicating the formation and the stable existence of Zn-O in $Zn_2P_2O_7$ sample and the disappearance of Zn-O in ZnO control during CO_2RR. (c) The change of the FE_{CO} ratio of FE_{CO}(ZnO) to FE_{CO}($Zn_2P_2O_7$) with time at various applied current densities in a flow cell reactor with 1.0 M KOH as the electrolyte. (d-f) Operando XAFS characterization of (d) the normalized Zn *K*-edge XANES spectra, (e) calculated ratio of Zn oxidation states from linear combination fitting with respect to time during 35 min of reaction and (f) the Fourier-transformed Zn *K*-edge EXAFS spectra under the CO_2 gas diffusion electrolysis condition at an applied current density of -50 mA cm^{-2} with 1.0 M KOH as the electrolyte.

The electrocatalytic performances of $Zn_2P_2O_7$ for CO_2RR were firstly evaluated in a standard three-electrode configuration in an H-cell (see details in the Supporting Information). As shown in Figure S9, the $Zn_2P_2O_7$ catalyst was tested over a range of potentials in 0.1 M $KHCO_3$, which showed a marked selectivity for CO at potentials from -0.9 to -1.30 V versus reversible hydrogen electrode (vs. RHE, all potentials were vs. RHE if not mentioned), with a peak FE_{CO} reaching 90.8 ± 0.8% and a j_{CO} of -5.5 mA cm^{-2} at -1.0 V. To further improve the electrocatalytic performance, a flow cell configuration was used to overcome the CO_2 mass-transport issue in the batch-type (*e.g.*, H-cell) electrolysis. Chronopotentiometric tests were conducted to motivate the CO_2 gas diffusion electrolysis at the constant *j* from -50 to -500 mA cm^{-2} (Figure S10). During the electrolysis, the obtained gas products were quantified by online gas chromatography (see more details in Supporting Information). In Figure 3a, current-dependent gas distribution results illustrate that $Zn_2P_2O_7$ exhibits high CO selectivities in the wide *j* range, with FE_{CO} of 88.5 ± 4.4%, 93.2 ± 0.4%, 98.9 ± 2.9%, 92.5 ± 2.1%, and 88.2 ± 4.5% at the *j* of -100, -200, -300, -400, and -500 mA cm^{-2}, respectively (the representative gas chromatography result is shown in Figure S11). This means that $Zn_2P_2O_7$ can deliver a high j_{CO} up to -441 mA cm^{-2}

^{2} at a low potential of -0.87 V. Considering the remarkable j_{CO} and corresponding potential, $Zn_2P_2O_7$ is among the best catalysts of the Zn-based materials (most of which with $|j_{CO}|$ < 50 mA cm^{-2}) and the developed CO_2-to-CO electrocatalysts (Figure 3b and Table S1)[5b,25]. This performance of $Zn_2P_2O_7$ proves that it can be potentially further used for industrial-current electrolysis with low energy input. With this in mind, we constructed a two-electrode anion MEA electrolysis system, using $Zn_2P_2O_7$ as cathode electrocatalysts and NiFe layered double hydroxide (LDH) on Ni foam as anode electrocatalysts[26]. In Figure 3c, the cyclic voltammetric curves show the obvious redox peaks when the applied cell voltage is lower than 2.0 V, which might be attributed to redox reactions of $Zn_2P_2O_7$. Constant j electrolysis was carried out to evaluate the selectivity and applied voltage of the $Zn_2P_2O_7$ catalyst (Figure S12, S13). In Figure 3d, $Zn_2P_2O_7$ exhibits high EE of 52.3%, 58.0%, and 45.0% at the j of -50, -100, and -150 mA cm^{-2}, respectively, with optimal FE_{CO} of 93.9% at the j of -100 mA cm^{-2} (see details in Supporting Information). This high EE is also comparable to the classic precious and nonprecious electrocatalysts at similar current densities, such as Ag, Au, and CoPc-based materials (Figure 3e and Table S2)[4,9b,27]. The long-term stability test of $Zn_2P_2O_7$ at the j of -100 mA cm^{-2} was also implemented in the MEA configuration (Figure 3f). The FE_{CO} gradually increased from 84.0 to 92.5% during 60 min of electrolysis and kept over 90% for more than 340 min. The slightly decreased FE_{CO} after 350 min might be attributed to the salt accumulation, corrosion of the gas diffusion layer (GDL), and degradation of the membrane. It is also mentionable that no obvious increase of energy input was found, and the applied cell voltage nearly remained the same.

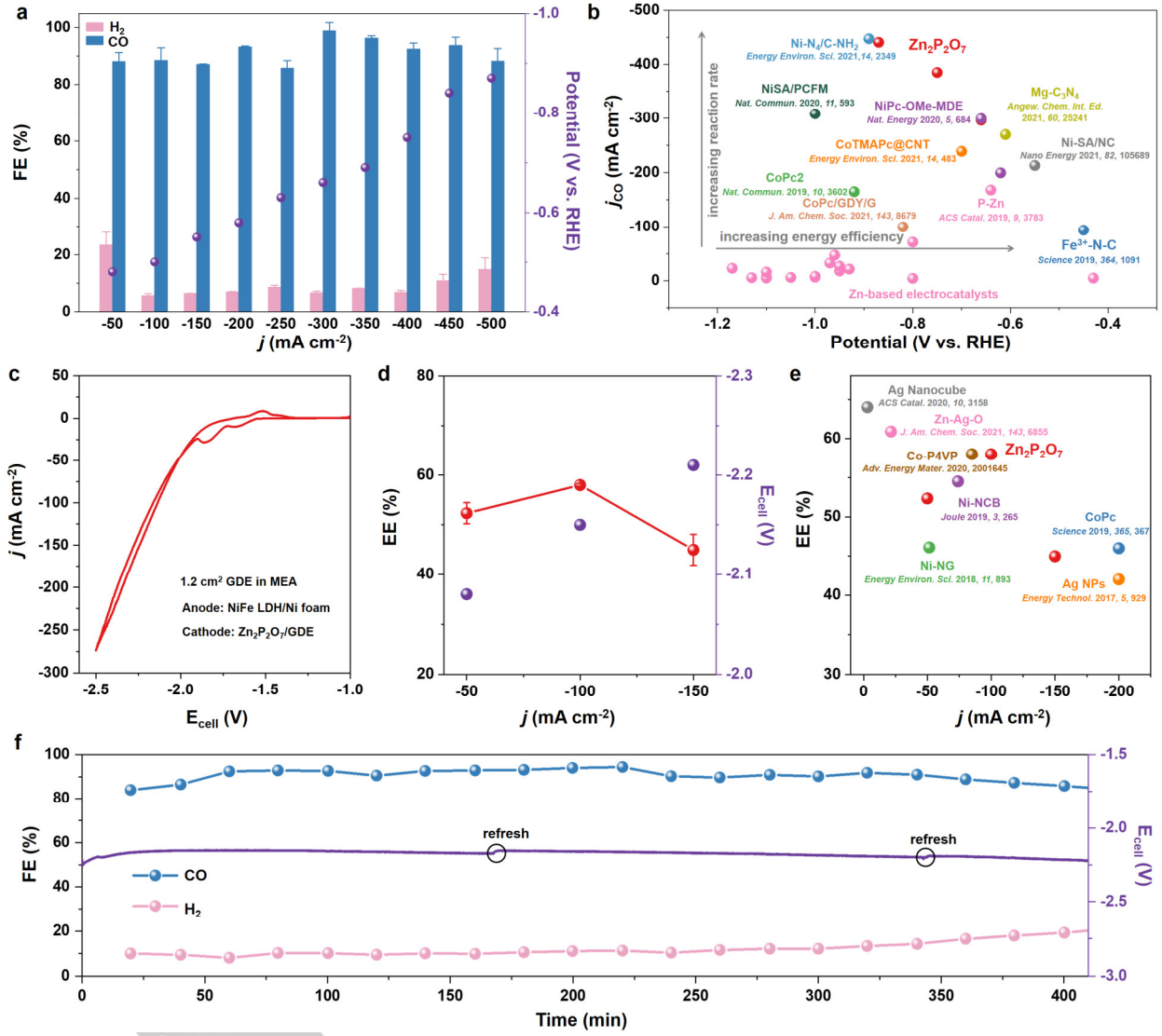

Figure 3. Electrocatalytic performance of $Zn_2P_2O_7$ catalyst. (a) Faradaic efficiencies for products and the corresponding potentials over $Zn_2P_2O_7$ at various applied current densities in a flow cell reactor with 2.0 M KOH as the electrolyte. (b) Maximum j_{CO} and the corresponding potential of $Zn_2P_2O_7$, recently reported Zn-based CO_2RR catalysts and some outstanding CO_2-to-CO electrocatalysts. (c-f) Electrochemical performance evaluation of $Zn_2P_2O_7$ catalysts for CO_2RR using the MEA system in 1.0 M KOH. (c) LSV curves of $Zn_2P_2O_7$ catalysts with respect to RHE at a scan rate of 1 mV s^{-1}. (d) Energy efficiencies of CO on $Zn_2P_2O_7$ catalysts and corresponding cell voltages at various applied current densities. (e) Performance comparison between $Zn_2P_2O_7$ catalysts and previously reported representative electrocatalysts for CO_2-to-CO conversion. (f) Stability test of electrochemical CO_2 reduction during 400 min of electrolysis under the j of -100 mA cm^{-2}. Red dots represent FE_{H2}, blue dots represent for FE_{CO} and the cyan line represents the cell voltage curve.

10.1002/anie.202202298

RESEARCH ARTICLE

In the operando condition, the local active structure of the catalyst is different from the well-defined structural feature, which is always difficult to be traced because of its non-uniqueness. Aiming to search the possible local active structures of ZnO_x and obtain their general features with more excellent CO_2-to-CO conversion performance compared with Zn, the evolutionary-algorithm-based (EA) global optimization method in the USPEX program combined with the DFT level calculation in VASP code was conducted to locate the energetically stable amorphous ZnO_x from the global configuration space (Figure 4a, see details in Supporting Information)[28]. After 20 generations' evolution, 484 structures could be obtained, which were evaluated firstly through the formation energy (E_f, Figure 4b, see details in Supporting Information). From the searched results, more than one representative structure with optimal stabilities is randomly selected, which can primely reveal the general structural features of ZnO_x (structure I-VI, Figure 4b). All of them are less-crystalized with relatively irregular and distorted surface structures, and the metalloid hollow sites constituted by $Zn^{\delta+}$ (*i.e.*, three conterminal $Zn^{\delta+}$-$Zn^{\delta+}$ bonds) are their common typical local structural features. Here, we further calculated the Gibbs reaction energy (ΔG) of the leaching-out of the lattice oxygen in structure I as an example to examine the electrochemical stabilities of these ZnO_x structures (Figure S14, the calculation details are shown in Supporting Information). As ΔG is more positive, the leaching-out of the lattice oxygen is more difficult, implying the better stability of ZnO_x. From Figure S14, it is obvious that ZnO_x holds a more positive ΔG than ZnO, implying the more difficult reduction of the lattice oxygen on ZnO_x, *i.e.*, the more superior electrochemical stability of these ZnO_x at the applied potential.

To further clarify the reason for the excellent activity of ZnO_x catalyzing CO_2-to-CO, we took the structure I of ZnO_x as an example, and calculated the Gibbs reaction free energies of CO_2RR at 0 V (vs. RHE) on Zn and ZnO_x, respectively (the calculation details are shown in Supporting Information). As shown in Figure 4c, the Gibbs adsorption free energy for CO_2 on ZnO_x is relatively more negative than that on Zn (0.49 vs.1.34 eV), indicating the better activation of $Zn^{\delta+}$ sites for CO_2, which is a key step for CO_2RR. The easier adsorption and activation of CO_2 can contribute to the next $*CO_2$ hydrogenation process, as the lower whole energy profile of CO_2RR on ZnO_x compared with that on Zn catalyst illustrates. In order to further understand the intrinsic origin of high CO_2-to-CO catalytic activity on ZnO_x, we introduced the projected electron density of states (DOS) analysis of Zn^0 and $Zn^{\delta+}$ sites which have been demonstrated by bader charge analysis (0 vs. +0.81) on Zn and ZnO_x, respectively. Comparing the *d*-band centers of $Zn^{\delta+}$ and Zn^0 (-6.54 vs. -7.34 eV, the upper part of Figure 4d), we can find that the *d*-band center of $Zn^{\delta+}$ on ZnO_x is closer to the Fermi level than that of Zn^0 on Zn catalyst, suggesting that the electron on $Zn^{\delta+}$ more easily transfers to CO_2, thus promoting the adsorption and activation of CO_2 on ZnO_x. In general, ZnO_x exhibits a better catalytic activity on the metalloid hollow sites constituted with $Zn^{\delta+}$ compared with the hollow sites constituted with Zn^0 on Zn catalysts, which helps to activate CO_2 and leads to more feasible formations of *COOH and *CO.

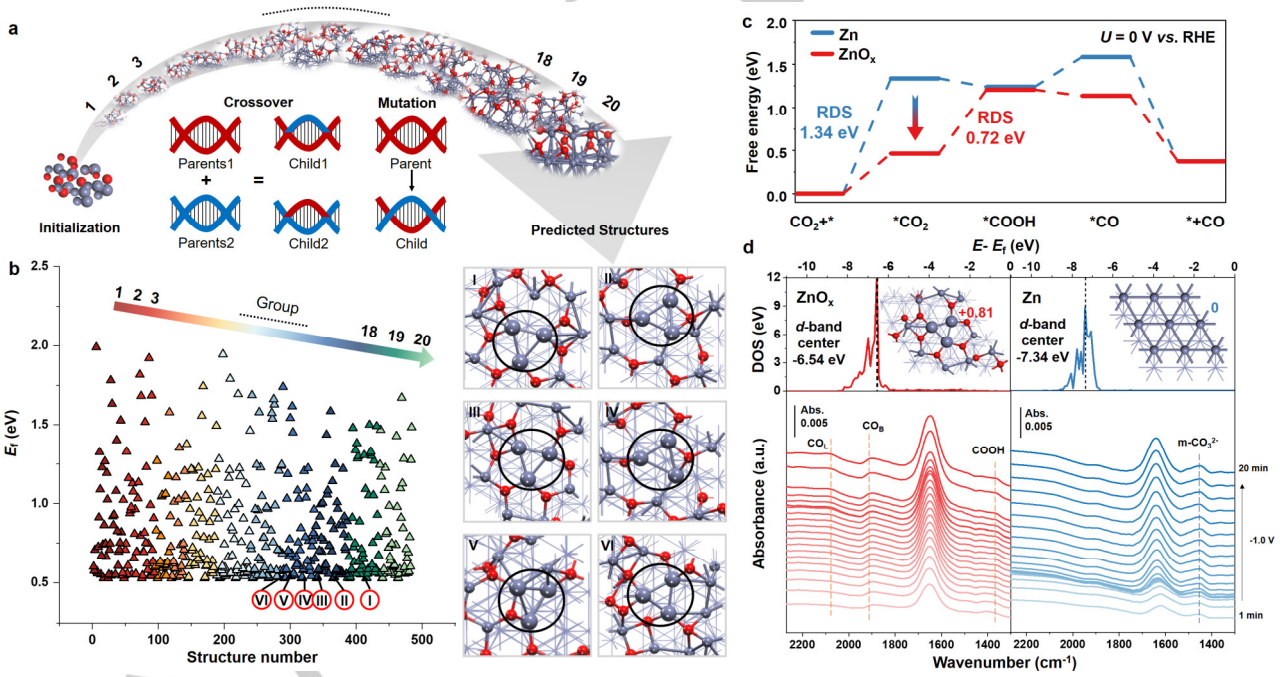

Figure 4. Theoretical study of ZnO_x for CO_2RR. (a) Screening process of ZnO_x based on EA global optimization method. (b) Formation energy of candidate structures of ZnO_x from USPEX and representative structures (I-VI) of ZnO_x with optimal stabilities. (c) Energy profiles of CO_2 to CO on Zn and ZnO_x at 0 V (vs. RHE), respectively. (d) Projected electron density of states (DOS) of *d* orbital, *d*-band center, and valence of Zn sites on Zn and ZnO_x (upper part); *In-situ* SEIRAS spectra of the $Zn_2P_2O_7$ and ZnO sample in CO_2-purged 0.1 M $KHCO_3$ electrolyte at -1.0 V in real-time condition (lower part).

Furthermore, we used *in-situ* SEIRAS to identify the intermediates formed on different Zn surfaces during CO_2RR, in order to experimentally understand the effect of the valence state of Zn surfaces on the CO_2RR mechanism (details in Supporting Information, Figure S15)[29]. As shown in the lower part of Figure 4d, peaks revealed at ~2085, ~1897, and ~1365 cm^{-1}

corresponding to atop-adsorbed CO (CO_L), bridge-adsorbed CO (CO_B), and carboxyl intermediate (*COOH) on the $Zn^{\delta+}$ surface appeared during CO_2RR, respectively[14a, 30]. In contrast, both *CO and *COOH were not obviously detected on the surface of the ZnO sample, which would be rapidly reduced to Zn^0 during CO_2 reduction. These results clearly demonstrate that the formations of *CO and *COOH, which are indispensable steps in producing CO, are more favorable on the $Zn^{\delta+}$ surface than those on the Zn^0 surface. Ultimately, the theoretical research in conjunction with *in-situ* SEIRAS study reveal that the formation of *CO and *COOH can be facilitated on $Zn_2P_2O_7$, indicating an improved CO_2-to-CO conversion due to the presence of the $Zn^{\delta+}$ metalloid hollow sites.

Conclusion

In conclusion, we have explored $Zn_2P_2O_7$ as an efficient CO_2-to-CO precatalyst *via* a facile sol-gel method, and unraveled that the active local structures of derived nonstoichiometric ZnO_x are the $Zn^{\delta+}$ metalloid hollow sites through structure characterization and EA global optimization method. DFT calculations and *in-situ* SEIRAS results further demonstrate that the special metalloid $Zn^{\delta+}$ hollow sites can promote the CO_2 activation and hydrogenation to *COOH during CO_2RR. Consequently, the operando-derived ZnO_x can deliver excellent catalytic performance with a high j_{CO} of -441 mA cm^{-2} at a low potential of ~870 mV, and a full-cell EE up to 58.0%. This work specifies a real active site and a clear structure-activity relationship for the precatalysts, which could provide guidance for designing ideal earth-abundant electrocatalysts for CO_2RR and many other related reactions of practical significance.

Acknowledgements

This work was financially supported by the International (Regional) Cooperation and Exchange Projects of the National Natural Science Foundation of China (51920105003), the National Natural Science Funds for Distinguished Young Scholars (51725201), the Innovation Program of Shanghai Municipal Education Commission (E00014), the National Natural Science Foundation of China (51902105, 21902048, 52103340), the Science and Technology Commission of Shanghai Municipality (21DZ1207101, 19YF1411600, 20QA1402400), the National Postdoctoral Program for Innovative Talents (BX20190113), and the Shanghai Engineering Research Center of Hierarchical Nanomaterials (18DZ2252400). Additional support was provided by the Feringa Nobel Prize Scientist Joint Research Center. The authors also thank the Frontiers Science Center for Materiobiology and Dynamic Chemistry. The authors also thank the crew of the BL14W1 beamline at the Shanghai Synchrotron Radiation Facility (SSRF) and the 1W1B beamline of Beijing Synchrotron Radiation Facility (BSRF) for their constructive assistance with the XAFS measurements and data analyses.

Keywords: active local structure • CO_2 reduction reaction • EA global optimization method • metalloid $Zn^{\delta+}$ • zinc pyrophosphate

[1] a) C. Hepburn, E. Adlen, J. Beddington, E. A. Carter, S. Fuss, N. Mac Dowell, J. C. Minx, P. Smith, C. K. Williams, *Nature* **2019**, *575*, 87−97; b) P. De Luna, C. Hahn, D. Higgins, S. A. Jaffer, T. F. Jaramillo, E. H. Sargent, *Science* **2019**, *364*, eaav3506.

[2] a) B. A. Rosen, A. Salehi-Khojin, M. R. Thorson, W. Zhu, D. T. Whipple, P. J. A. Kenis, R. I. Masel, *Science* **2011**, *334*, 643−644; b) C. Costentin, S. Drouet, M. Robert, J. M. Saveant, *Science* **2012**, *338*, 90−94; c) R. G. Mariano, K. McKelvey, H. S. White, M. W. Kanan, *Science* **2017**, *358*, 1187−1192.

[3] a) W. Zhu, R. Michalsky, Ö. Metin, H. Lv, S. Guo, C. J. Wright, X. Sun, A. A. Peterson, S. Sun, *J. Am. Chem. Soc.* **2013**, *135*, 16833−16836; b) M. Valenti, N. P. Prasad, R. Kas, D. Bohra, M. Ma, V. Balasubramanian, L. Chu, S. Gimenez, J. Bisquert, B. Dam, W. A. Smith, *ACS Catal.* **2019**, *9*, 3527−3536; c) X. Peng, S. G. Karakalos, W. E. Mustain, *ACS Appl. Mater. Inter.* **2018**, *10*, 1734−1742.

[4] S. Ren, D. Joulié, D. Salvatore, K. Torbensen, M. Wang, M. Robert, C. P. Berlinguette, *Science* **2019**, *365*, 367−369.

[5] a) X. Wang, X. Sang, C.-L. Dong, S. Yao, L. Shuai, J. Lu, B. Yang, Z. Li, L. Lei, M. Qiu, L. Dai, Y. Hou, *Angew. Chem. Int. Ed.* **2021**, *60*, 11959−11965; *Angew. Chem.* **2021**, *133*, 12066−12072. b) Z. Chen, X. Zhang, W. Liu, M. Jiao, K. Mou, X. Zhang, L. Liu, *Energy Environ. Sci.* **2021**, *14*, 2349−2356.

[6] D. U. Nielsen, X.-M. Hu, K. Daasbjerg, T. Skrydstrup, *Nat. Catal.* **2018**, *1*, 244−254.

[7] B. Qin, Y. Li, H. Fu, H. Wang, S. Chen, Z. Liu, F. Peng, *ACS Appl. Mater. Inter.* **2018**, *10*, 20530−20539.

[8] K. Liu, J. Wang, M. Shi, J. Yan, Q. Jiang, *Adv. Energy Mater.* **2019**, *9*, 1900276.

[9] a) W. Zhu, L. Zhang, S. Liu, A. Li, X. Yuan, C. Hu, G. Zhang, W. Deng, K. Zang, J. Luo, Y. Zhu, M. Gu, Z.-J. Zhao, J. Gong, *Angew. Chem. Int. Ed.* **2020**, *59*, 12664−12668. *Angew. Chem.* **2020**, *132*, 12764–12768; b) Z. Zhang, G. Wen, D. Luo, B. Ren, Y. Zhu, R. Gao, H. Dou, G. Sun, M. Feng, Z. Bai, A. Yu, Z. Chen, *J. Am. Chem. Soc.* **2021**, *143*, 6855−6864.

[10] J. Chen, Z. Li, X. Wang, X. Sang, S. Zheng, S. Liu, B. Yang, Q. Zhang, L. Lei, L. Dai, Y. Hou, *Angew. Chem. Int. Ed.* **2022**, *61*, e202111683. *Angew. Chem.* **2022**, *134*, e202111683.

[11] Z. Geng, X. Kong, W. Chen, H. Su, Y. Liu, F. Cai, G. Wang, J. Zeng, *Angew. Chem. Int. Ed.* **2018**, *57*, 6054−6059; *Angew. Chem.* **2018**, *130*, 6162−6167.

[12] T. A. Al-Attas, N. N. Marei, X. Yong, N. G. Yasri, V. Thangadurai, G. Shimizu, S. Siahrostami, M. G. Kibria, *ACS Catal.* **2021**, *11*, 7350–7357.

[13] H. S. Jeon, I. Sinev, F. Scholten, N. J. Divins, I. Zegkinoglou, L. Pielsticker, B. R. Cuenya, *J. Am. Chem. Soc.* **2018**, *140*, 9383−9386.

[14] a) T.-C. Chou, C.-C. Chang, H.-L. Yu, W.-Y. Yu, C.-L. Dong, J.-J. Velasco-Vélez, C.-H. Chuang, L.-C. Chen, J.-F. Lee, J.-M. Chen, H.-L. Wu, *J. Am. Chem. Soc.* **2020**, *142*, 2857−2867; b) L. Wang, Y. Zhu, Y. Wen, S. Li, C. Cui, F. Ni, Y. Liu, H. Lin, Y. Li, H. Peng, B. Zhang, *Angew. Chem. Int. Ed.* **2021**, *60*, 10577−10582; *Angew. Chem.* **2021**, *133*, 10671−10676. c) X. Zheng, P. De Luna, F. P. García de Arquer, B. Zhang, N. Becknell, M. B. Ross, Y. Li, M. N. Banis, Y. Li, M. Liu, O. Voznyy, C. T. Dinh, T. Zhuang, P. Stadler, Y. Cui, X. Du, P. Yang, E. H. Sargent, *Joule* **2017**, *1*, 794−805.

[15] S. H. Lee, J. C. Lin, M. Farmand, A. T. Landers, J. T. Feaster, J. E. Avilés Acosta, J. W. Beeman, Y. Ye, J. Yano, A. Mehta, R. C. Davis, T. F. Jaramillo, C. Hahn, W. S. Drisdell, *J. Am. Chem. Soc.* **2021**. *143*, 588−592.

[16] S. Li, S. Zhao, X. Lu, M. Ceccato, X.-M. Hu, A. Roldan, J. Catalano, M. Liu, T. Skrydstrup, K. Daasbjerg, *Angew. Chem. Int. Ed.* **2021**, *60*, 22826−22832. *Angew. Chem.* **2021**, *133*, 23008–23014.

[17] a) N. Heidary, K. H. Ly, N. Kornienko, *Nano Lett.* **2019**, *19*, 4817−4826; b) Y. Y. Birdja, E. Pérez-Gallent, M. C. Figueiredo, A. J. Göttle, F. Calle-Vallejo, M. T. M. Koper, *Nat. Energy* **2019**, *4*, 732−745.

[18] H. Kim, J. Park, I. Park, K. Jin, S. E. Jerng, S. H. Kim, K. T. Nam, K. Kang, *Nat. Commun.* **2015**, *6*, 8253.

[19] S. K. Gupta, M. Mohapatra, S. V. Godbole, V. Natarajan, *RSC Adv.* **2013**, *3*, 20046−20053.

[20] F. Yang, P. Song, X. Liu, B. Mei, W. Xing, Z. Jiang, L. Gu, W. Xu, *Angew. Chem. Int. Ed.* **2018**, *57*, 12303–12307; *Angew. Chem.* **2018**, *130*, 12483–12487.

[21] Y. Chang, N.-E. Shi, S. Zhao, D. Xu, C. Liu, Y.-J. Tang, Z. Dai, Y.-Q. Lan, M. Han, J. Bao, *ACS Appl. Mater. Inter.* **2016**, *8*, 22534−22544.

[22] B. Boonchom, R. Baitahe, *Mater. Lett.* **2009**, *63*, 2218−2220.

[23] a) Z. Yin, S. Wu, X. Zhou, X. Huang, Q. Zhang, F. Boey, H. Zhang, *Small* **2010**, *6*, 307−312; b) R. Cuscó, E. Alarcón-Lladó, J. Ibáñez, L. Artús, J. Jiménez, B. Wang, M. J. Callahan, *Phys. Rev. B* **2007**, *75*, 165202.

[24] H.-L. Jiang, Q. Yang, C.-C. Yang, C.-H. Lin, *Angew. Chem. Int. Ed.* **2019**, *58*, 3511-3515; *Angew. Chem.* **2019**, *131*, 3549−3553.

[25] a) W. Luo, J. Zhang, M. Li, A. Züttel, *ACS Catal.* **2019**, *9*, 3783−3791; b) J. Gu, C.-S. Hsu, L. Bai, H. M. Chen, X. Hu, *Science* **2019**, *364*, 1091−1094; c) X. Zhang, Y. Wang, M. Gu, M. Wang, Z. Zhang, W. Pan, Z. Jiang, H. Zheng, M. Lucero, H. Wang, G. E. Sterbinsky, Q. Ma, Y.-G. Wang, Z. Feng, J. Li, H. Dai, Y. Liang, *Nat. Energy* **2020**, *5*, 684−692; d) J. Su, J.-J. Zhang, J. Chen, Y. Song, L. Huang, M. Zhu, B. I. Yakobson, B. Z. Tang, R. Ye, *Energy Environ. Sci.* **2021**, *14*, 483−492; e) X. Wang, S. Ding, T. Yue, Y. Zhu, M. Fang, X. Li, G. Xiao, Y. Zhu, L. Dai, *Nano Energy* **2021**, *82*, 105689; f) H. Gu, L. Zhong, G. Shi, J. Li, K. Yu, J. Li, S. Zhang, C. Zhu, S. Chen, C. Yang, Y. Kong, C. Chen, S. Li, J. Zhang, L. Zhang, *J. Am. Chem. Soc.* **2021**, *143*, 8679−8688; g) Q. Wang, K. Liu, J. Fu, C. Cai, H. Li, Y. Long, S. Chen, B. Liu, H. Li, W. Li, X. Qiu, N. Zhang, J. Hu, H. Pan, M. Liu, *Angew. Chem. Int. Ed.* **2021**, *60*, 25241-25245; *Angew. Chem.* **2021**, *133*, 25445−25449; h) M. Wang, K. Torbensen, D. Salvatore, S. Ren, D. Joulié, F. Dumoulin, D. Mendoza, B. Lassalle-Kaiser, U. Işci, C. P. Berlinguette, M. Robert, *Nat. Commun.* **2019**, *10*, 3602; i) H. Yang, Q. Lin, C. Zhang, X. Yu, Z. Cheng, G. Li, Q. Hu, X. Ren, Q. Zhang, J. Liu, C. He, *Nat. Commun.* **2020**, *11*, 593.

[26] X. Lu, C. Zhao, *Nat. Commun.* **2015**, *6*, 6616.

[27] a) T. Zheng, K. Jiang, N. Ta, Y. Hu, J. Zeng, J. Liu, H. Wang, *Joule* **2019**, *3*, 265−278; b) K. Jiang, S. Siahrostami, T. Zheng, Y. Hu, S. Hwang, E. Stavitski, Y. Peng, J. Dynes, M. Gangisetty, D. Su, K. Attenkofer, H. Wang, *Energy Environ. Sci.* **2018**, *11*, 893−903; c) R. B. Kutz, Q. Chen, H. Yang, S. D. Sajjad, Z. Liu, I. R. Masel, *Energy Technol.* **2017**, *5*, 929−936; d) S. Liu, C. Sun, J. Xiao, J.-L. Luo, *ACS Catal.* **2020**, *10*, 3158−3163; e) N. Fujinuma, A. Ikoma, S. E. Lofland, *Adv. Energy Mater.* **2020**, *10*, 2001645.

[28] a) A. R. Oganov, C. W. Glass, *J. Chem. Phys.* **2006**, *124*, 244704; b) A. R. O. A. O. Lyakhov, M. Valle, *Acc. Chem. Res.* **2011**, *44*, p.227−237; c) Q. Wang, A. R. Oganov, Z. Qiang, X. F. Zhou, *Phys. Rev. Lett.* **2014**, *113*, 266101; d) Z. Qiang, L. Li, A. R. Oganov, P. B. Allen, *Phys. Rev. B* **2013**, *87*, 195317.

[29] J. Heyes, M. Dunwell, B. Xu, *J. Phys. Chem. C* **2016**, *120*, 17334−17341.

[30] a) S. Zhu, B. Jiang, W.-B. Cai, M. Shao, *J. Am. Chem. Soc.* **2017**, *139*, 15664−15667; b) C. M. Gunathunge, V. J. Ovalle, Y. Li, M. J. Janik, M. M. Waegele, *ACS Catal.* **2018**, *8*, 7507−7516.

10.1002/anie.202202298

WILEY-VCH

RESEARCH ARTICLE

Entry for the Table of Contents

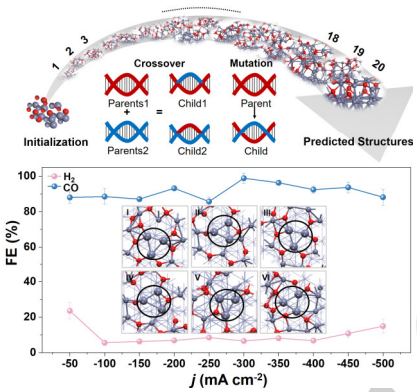

The operando $Zn^{\delta+}$ metalloid hollow sites of stable nonstoichiometric ZnO_x derived from $Zn_2P_2O_7$ were unraveled to be the real active site structures through structure characterizations in conjunction with evolutionary-algorithm-based global optimization method, which delivered excellent CO_2-to-CO conversion performance.